Carbonated balsa-based shape-stable phase change materials with photothermal conversion and application in greenhouse

Nan Zhang [a], Xiyu Pan [a,d], Zhaoli Zhang [a,*], Yanping Yuan [a], Muhammad Sultan [b], Shady Attia [c]

[a] School of Mechanical Engineering, Southwest Jiaotong University, Chengdu, 610031, China
[b] Department of Agricultural Engineering, Bahauddin Zakariya University, Multan, 60800, Pakistan
[c] Sustainable Building Design Lab, Dept. UEE, Faculty of Applied Sciences, University of Liège, Liège, 4000, Belgium
[d] Chengdu Architectural Design & Research Institute Co.,Ltd, Chengdu, 610041, China

ABSTRACT

Greenhouse enables to promote plant yield through creating optimal environment. Efficient solar energy conversion and storage is a promising strategy to address energy shortage issue of greenhouse in winter. This paper prepares form-stable composite phase change materials (PCMs) to store solar energy efficiently. Lightweight and porous balsa wood subjected to high-temperature carbonization is designed to simultaneously solve the liquid leakage, enhance the thermal conductivity, and improve the photothermal conversion and thermal energy storage of PCM. OP44E and SEBS are utilized as PCM and thickener, followed by vacuum impregnation into the carbonized balsa wood (CW). Results indicate that carbon content of CW increases with the augment of carbonization temperature. Shaping effects of CW and SEBS endow composite PCMs to have highest adsorption rate of 92.7 wt% with enthalpy over 190 J/g. Composite PCMs reveal reliable thermal properties and thermal stability below 100 °C. Composite PCMs have photothermal conversion larger than 88 % under a xenon lamp radiation. Temperature of PCMs on the shallow layer is higher owing to its photothermal conversion capacity. Greenhouse test indicates that CW/OP44E/SEBS greenhouse gains higher PCM temperature of 71.5 °C at 70 min, compared to 40.3 °C in empty and OP44E/SEBS cases. CW/OP44E/SEBS greenhouse maintaining indoor temperature over 20 °C lasts 15.3 min longer than empty and OP44E/SEBS greenhouses. In addition, form-stable composite PCMs featured with excellent thermal stability and photothermal conversion are capable of maintaining stable indoor temperature of greenhouse, indicating potential in the field of agricultural building temperature regulation.

1. Introduction

People are concerned more about living quality and the demands of healthier and fresher vegetables and fruits continue to increase [1]. Greenhouse has advantages of off-season, short cycle and high yield, which is suitable to vegetable and fruit production [2]. The greenhouse is gradually evolved into an indispensable form for development of modern agricultural production. Whereas, low temperature in sunlight greenhouse during winter results in quality and yield decline of vegetables and fruits [3]. Exploring measures to improve winter thermal performance is essential to development of greenhouse.

As PCMs are widely utilized as efficient energy storage media in the field of building energy conservation due to their excellent heat storage and release capabilities within an almost constant temperature range. It

is a positive way to reduce energy consumption and improve environmental problems by using PCMs. Bao et al. [4] found that compared the room without PCMs, the room with PCM walls consumes less electricity. And the payback period of using PCM in Hong Kong and Changsha are about 18.3 and 8.4 years, respectively, which are much smaller than the average life (60 years) for the residential building. Wijesuriya et al. [5] proposed an optimal PCM-integrated envelope which can provide annual energy savings up to 10.8 % in a lightweight residential building located in Baltimore, MD. As a special form of building, the agricultural greenhouses are increasingly using PCMs to decrease the energy consumption [6]. Zhu et al. [7] reviewed the current status and development of research on PCMs in greenhouses in this year. From the review, it is important to select and modify the PCMs to meet the temperature range of greenhouse, and the application form of PCM used in the

* Corresponding author.
E-mail address: zzlyzhang@swjtu.edu.cn (Z. Zhang).

greenhouse. According to the material type, PCMs can be roughly classified as organic, inorganic and hybrid PCMs. Organic paraffin is one of the most commonly used solid-liquid PCMs in consideration of the high energy storage capacity and relatively low cost [8–10]. And paraffin has been proven to be applicable in greenhouse [11]. Inevitably, paraffin suffers from the liquid leakage during phase transition, low thermal conductivity and no photothermal conversion function, then limiting the further development of PCMs.

Recent years witness an increasing number of studies towards the shape stability of solid-liquid PCMs. Among them, the novel shaped PCM with biomass as the support skeleton is gradually gaining attention due to its wide sources, environmental friendliness and cost effectiveness [12,13]. The porous structure of biomass provides innate advantage to the attachment of PCMs. Nam et al. [14] used the hard core and outer bark of wood as s a support material for stabilizing PCM, and it found that the structural and chemical compositions of the core and bark has a significant influence on PCM impregnation. The shape-stabilized PCMs (SSPCMs) with cork shows a 49 % efficiency compared with the PCM. Sun et al. [15] treated the wood with delignification and used it as supporting materials to fabricate the SSPCMs. The maximum impregnation rate of PCM in the delignified wood DW is as high as 76 wt%. Moreover, in order to simultaneously improve the shortages of liquid leakage and poor thermal conductivity of PCM, biochar obtained by the carbonization treatment of biomass are considered a good supporting material. Biochar is found to have many grooves on surface and porous networks inside the structure, which absorbs PCMs to prevent from its liquid leakage [16–18]. Yang et al. [19] found that the carbonized logs had a stable tubular structure. And the maximum adsorption ratio for PCM is 81 wt%. Lv et al. [20] utilized five waste biomass materials as precursors to produce biochar samples for loading PCMs. And the activated biochar derived from corncob (CC) shows remarkable textural characteristic, the loading capacity of CC for PCM as high as 85 %. Other possible biomass including wood [21–23], fruit [24–26], vegetable [17, 27], etc. Also demonstrated three-dimensional structure after carbonization treatment. Theoretically, the porous biochar is able to provide various acting forces (capillary force, surface tension, hydrogen bonding force, etc.) to stabilize the PCM embedded inside the pore of the carrier. It can serve as an excellent shaping carrier for fabricating composite PCMs.

Similar to carbon materials, biochar not only has admirable thermal conductivity and adsorption capacity, but also has strong light capture and photothermal conversion capability. Thus, the biochar-based composite PCM can directly store the solar energy. Xiao et al. [28] used Ag modified loofah-based porous carbon as supporting material to prepare the photo-thermal conversion composite PCMs. The nano-Ag not only considerably improved the thermal conductivity, but also significantly improved the photo-thermal conversion efficiency. Wei et al. [29] treated succulent plants into carbon aerogels and then impregnated paraffin. The photothermal conversion efficiency could reach as high as 82 %. Our previous study [30] also carbonized porous wood for the sake of adsorbing paraffin and the photothermal conversion efficiency could reach 90 % under the irradiation of a 100 mW/cm^2 xenon lamp. Therefore, the use of biochar to improve photothermal conversion performance is of particularly attractive in the photothermal capture and conversion.

Available previous studies indicate that PCMs will still leak from the surface open pore structure of porous supporting materials due to gravity during long-term operation. Auxiliary substances are suggested to further improve adsorption effect of the pore structure on PCMs [31–33]. Chen et al. [34] coated graphite on exterior of the carbide wood-based composite PCM to encapsulate the sample as a whole in order to prevent leakage of PCMs. Chen et al. [35] selected lightweight marco-porous carbonized melamine sponge (CMS) as supporting material, and PCM was impregnated into CMS firstly. In order to solve the leakage problem, the polyurethane thin-layer as shell to macro-encapsulate the CMS/PCM. Moreover, our previous work has

conformed that increasing the viscosity of PCM to reduce their flow-ability can also solve the leakage problem [36]. Styrene-b-(ethylene-co-butylene)-b-styrene (SEBS) comprises resin blocks and rubber blocks can store paraffin in its rubber blocks, while the resin blocks to form the crosslinked network structure. SEBS shows a good solubility with paraffin and it has been used assist in solving the leakage problem of paraffin [36–38].

Based on the above review, this paper aims to design a facile method to prepare a composite PCMs that can simultaneously solve the liquid leakage, enhance the thermal conductivity, and improve the photothermal conversion and thermal energy storage of PCM. So, SEBS working as the thickener was used to pretreat paraffin OP44E prior to compound with carbonized porous biomass. Carbonated balsa wood was utilized to supply porous supporting structure together with outstanding photothermal conversation and high thermal conductivity. Comprehensive performance of prepared composite PCMs was characterized via morphology and structure, thermophysical properties and stability. Photothermal conversion performance was evaluated under a xenon lamp radiation. Subsequent small-scale experiments compared temperature performance of greenhouses with and without composite PCMs, practically analyzing the application of composite PCMs.

2. Materials and experiments

2.1. Materials

Balsa wood (BW) used as carbon source was provided by a wood processing plant (Zaozhuang, China). The paraffin wax (OP44E, melting temperature: 41.5 °C, latent heat:234.7 J/g) used as PCM was provided by Ruhr New Materials Technology Co., Ltd (Hangzhou, China). SEBS applied as the thickening agent was supplied by Corten Polymer Trading Co., Ltd (Shanghai, China). Deionized water, sodium sulfite (NaSO$_3$, content ≥97 %) and Sodium hydroxide (NaOH, content ≥98 %) used in delignification were all bought from Kelong Chemical Reagents Co., Ltd (Chengdu, China). CW was obtained by a series of delignification, freeze-drying, and carbonization of BW. All of the reagents were utilized directly without further purification.

2.2. Preparation of CW/OP44E/SEBS composite PCMs

2.2.1. Preparation of CW

BW was firstly treated by delignification, freeze-drying, and carbonization to prepare the CW, according to the detailed treatment processing listed in our previous study [30]. In order to obtain the CW with various carbon contents and hierarchical structures, the carbonization treatment temperatures were respectively set as 300 °C, 500 °C, 700 °C and 900 °C, followed by heating duration of 1 h. The corresponding obtained CWs were recorded as CW300, CW500, CW700 and CW900, which would be used as supporting materials to prepare the composite PCMs.

2.2.2. Preparation of composite PCMs

As for the PCM, the paraffin OP44E and 5 wt% SEBS were intensively blended in an oil bath at 180 °C to form a transparent cross-linked mixture. The CWs were immersed into the melted OP44E/SEBS mixture under negative pressure of −0.08 MPa for 3 h, ensuring the CW pores were filled with OP44E/SEBS as much as possible.

The CW/OP44E/SEBS composite PCMs were obtained after cooling down to room temperature. The excess OP44E/SEBS was slowly heated into a liquid state by a hotplate, and the liquid OP44E/SEBS on the surface of the composite PCMs can be carefully removed by the adsorption of a filter paper. The CW/OP44E/SEBS composite PCMs adopting CW300, CW500, CW700, and CW900 as supporting materials were individually noted as CW300/OP44E/SEBS, CW500/OP44E/SEBS, CW700/OP44E/SEBS, and CW900/OP44E/SEBS for ease of simplification. Schematic diagram of CW/OP44E/SEBS composite PCMs

preparation is shown in Fig. 1.

2.3. Characterization

The microstructure of BW, CW and composite PCMs was observed by an electronic scanning microscope (SEM, Thermo Fisher FEI Inspect F) and the elemental energy spectra were performed for selected surface of CWs. The parameters of CW pore structure were determined by a mercury intrusion porosimeter (MIP, Micromeritics AutoPore IV 9500). The chemical property of composite PCMs was tested by a Fourier transform infrared spectrometer (FT-IR, Thermo Fisher Nicolet iS50) in the range of 400~4000^{-1} nm under the total reflection mode. The crystal structure of PCMs was characterized by an X-ray Diffraction (XRD, PANalytical B.V. Empyrean) in the range of 10~80°. A laser confocal Raman spectrometer (Raman, HORIBA Lab RAM HREvolution) was employed to test the molecular structure of CW in the range of 400~2000 cm^{-1} with a laser wavelength of 532 nm. The absorbance of the samples was analyzed by a UV–Vis–NIR spectrometer (Shimadzu UV-3600) over a wavelength range of 200~800 nm.

Thermal properties of PCMs were measured by a differential scanning calorimeter (DSC, TA Q20). Samples were heated and cooled over the temperature range of 10~70 °C at a rate of 5 °C/min for three times. The average results were labeled as thermophysical properties. A thermal gravimetric analyzer (TGA, Mettler Toledo TGA/DSC3+) was used for thermal stability testing from room temperature to 800 °C at a heating rate of 10 °C/min under nitrogen atmosphere. Thermal conductivity of the sample was tested by using a laser thermal conductivity meter (NETZSCH LFA 467). And the sample was pretreated into a square sheet with 10 mm length and 2 mm thickness.

The stability of PCMs was investigated by three methods. (1) Paraffin OP44E and OP44E/SEBS were packed into two glass vials that were heated to 80 °C to observe flowability of the PCMs; (2) Shape stability of the prepared CW/OP44E/SEBS composite PCMs was evaluated by a leakage test. The samples were placed on filter papers under 80 °C and weighed every 10 h until 160 h. The leakage rate was calculated as the change rate of PCM mass before and after the test; (3) PCMs were subjected to 200 endothermic/exothermic cycles using a constant temperature metal bath (Thermal Q CHB-T2-E). The bath was programmed in the temperature range of 10~70 °C and maintained at 10 °C and 70 °C for 5 min. Variation of thermal properties for PCMs before and after the thermal cycle was adopted to evaluate their thermal reliability.

The photothermal conversion determination was divided into two parts. First, the sample (1 cm × 1 cm × 2 cm) embedded in a pearl cotton insulation container was placed directly below a xenon lamp (Aulight CEL-S500/350) at an operating power of 100 mW/cm^2. The real-time temperature of sample was recorded with a K-type thermocouple set in the center of the sample during light on and off periods. An infrared thermographer (Testo 890) was also used to visualize the temperature contour of sample when the xenon lamp was turned on in order to highlight photothermal conversion of composite PCMs.

3. Results and discussion

3.1. Morphology and structure

Fig. 2 contours the microscopic morphology of CW700 and CW700/OP44E/SEBS through SEM test. SEM images of CW700 in cross-section and vertical-section at magnification of × 100 in Fig. 2 (a) and (e) show that CW700 has multilayer pore structure characterized by macropores-mesopores-micropores. The macropores are formed by ducts scattered inside of the BW. Pores of the tubular cell structure are closely arranged and much smaller than that of ducts. The cross-sections of pores are irregular polygon without inclusions as illustrated in Fig. 2 (b) and (f). High resolution SEM images of Fig. 2 (c) and (g) indicate that the pore wall thickness is around 0.5 μm after chemical delignification and carbonization. It is apparent that there are a large number of small
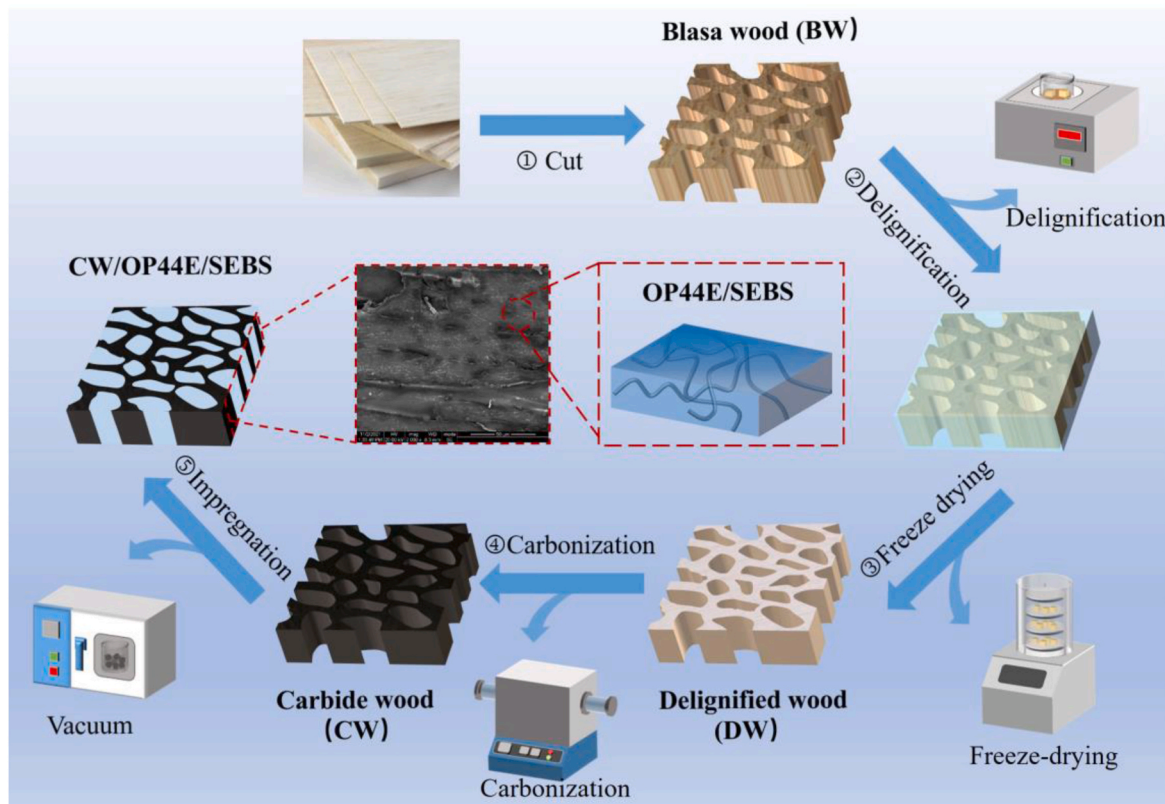

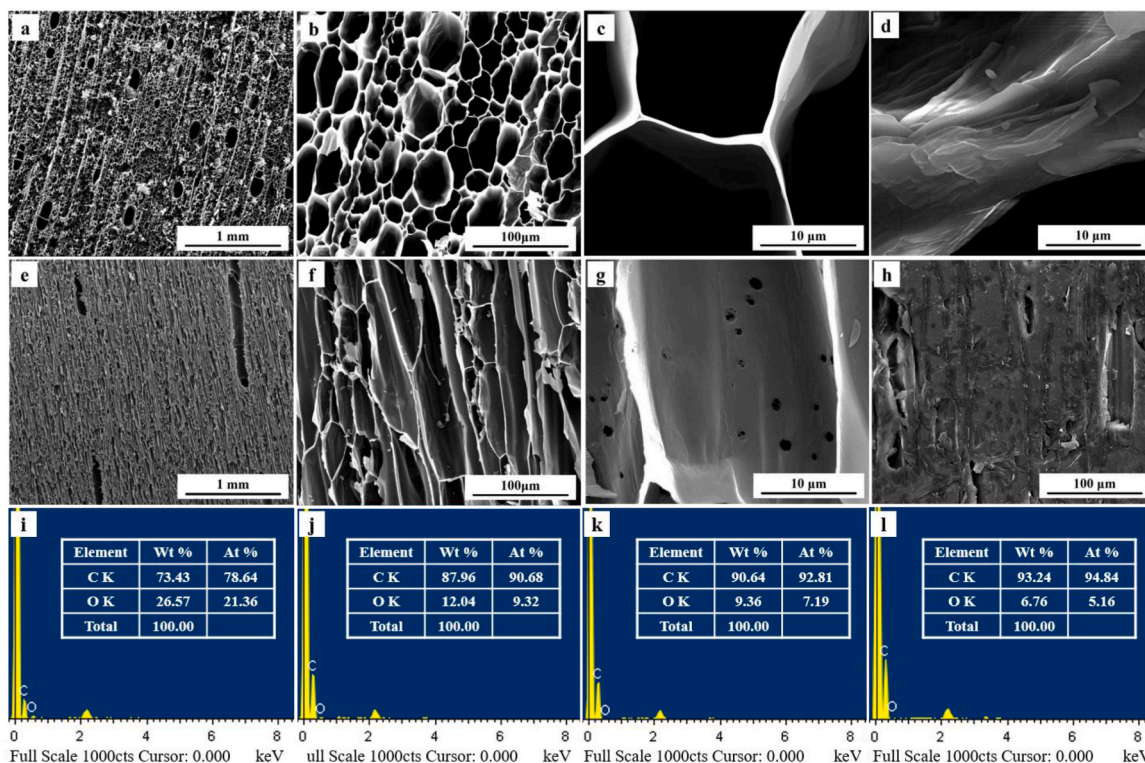**Fig. 1.** Schematic diagram of CW/OP44E/SEBS preparation.

Fig. 2. SEM images of CW700 (a)–(c) Cross-section, (e)–(g) Vertical section and CW700/OP44E/SEBS (d) Cross-section, (h) Vertical section; EDS spectra of CWs (i)–(l).

pores on surface of the wall, which is favorable to enhance the penetration between the original pores. Moreover, CW300, CW500 and CW900 also have the similar pore structures. For the sake of brevity, the SEM images of these three samples are not shown in the manuscript.

Fig. 2 (d) and (h) show the SEM images of CW700/OP44E/SEBS. It can be found that OP44E/SEBS is tightly adhered to the interior wall of CW700, and completely filled into the pore structure of CW700. EDS results in Fig. 2 (i)–(l) reveal that the C and O percentages of CW at
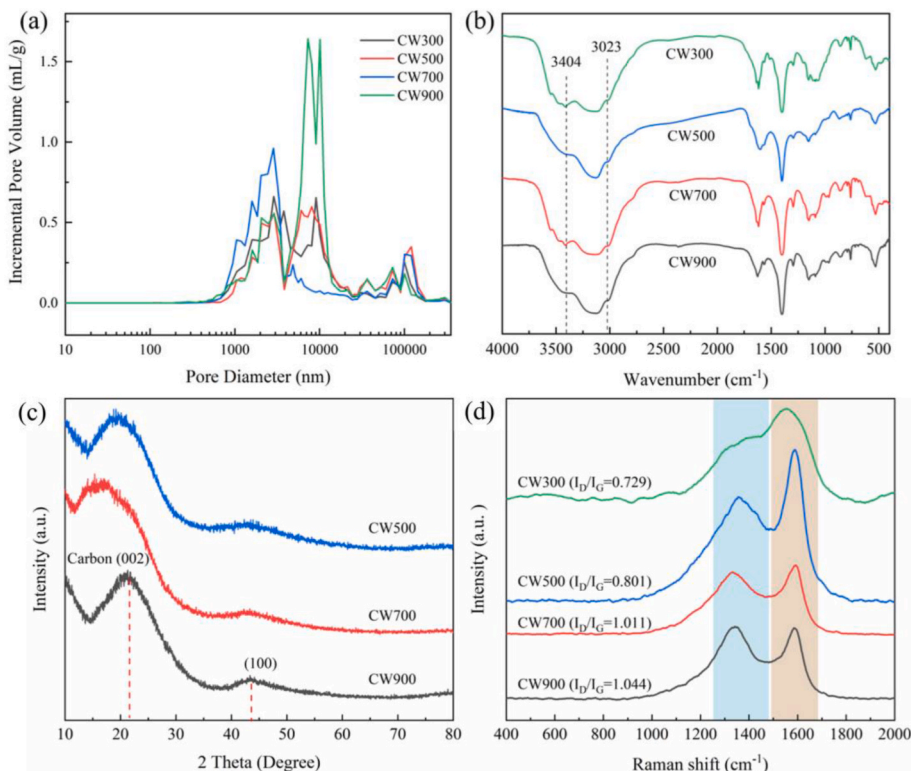

Fig. 3. Structural parameters of CWs. (a) Pore diameter distribution; (b) FT-IR; (c) XRD and (d) Raman spectrum.

different carbonation temperatures. Volatile substances (CO_2, CH_4, CO, etc.) can be removed in the high-temperature pyrolysis process, remaining the finial products of carbon materials. The sp^2 hybridized carbon atoms increase with the augment of carbonization temperature, which is beneficial to the transformation of wood to graphitization [39]. The carbon content of CW300 is merely 78.64 % and separately rises to 78.64 %, 90.68 %, 92.81 %, and 94.84 % in terms of CW500, CW700, and CW900.

Fig. 3 (a) shows that the pore size of CWs are mainly concentrated in the range of 160~11000 nm. Porosity, specific surface and pore volume of CWs are summarized in Table 1. It can be found that higher temperature enables to fasten carbonization rate, which then results in larger porosity, specific surface area and pore volume of CWs. The porosity of CWs increases from 88.61 % to 93.45 % as carbonization temperature rises from 300 to 900 °C. The rich pore structure of CW produces excellent adsorption capacity to OP44E/SEBS and has positive effect to thermal conductivity of composite PCMs. The FT-IR spectral profiles of CWs are shown in Fig. 3 (b). The diffraction peak located at 3404 cm^{-1} belongs to the stretching vibration of the hydroxyl group –OH, and the absorption peak near 3023 cm^{-1} is corresponding to the stretching vibration of methyl group –CH_3. The intensity of the absorption peak (hydroxyl group at 3404 cm^{-1}) gradually decreases with growth of the carbonization temperature, indicating that its dimensional stability can be well maintained during carbonization.

Fig. 3 (c) states that the CWs have two characteristic diffraction peaks at 21.6° and 43.5° in terms of XRD patterns, which is attributed to the carbon (002) and (100) planes, respectively [40,41]. It can be seen that the half-peak width of carbon (002) plane becomes narrower, while characteristic diffraction peak of the carbon (100) plane increases with augment of carbonization temperature, indicating that the physical phase of CW changes and its crystallinity increases at elevated temperature. The Raman spectra are shown in Fig. 3 (d). Graphitic characteristic peaks of D-band and G-band appeared at about 1340 cm^{-1} and 1588 cm^{-1} are corresponding to sp^3 for amorphous carbon and sp^2 for characterized graphitization, respectively [42]. Both the disordered and graphitic carbons cause the I_D/I_G ratio increase with growth of CW carbonization temperature.

FT-IR spectroscopy was performed to further analyze the chemical composition of SEBS and OP44E and their interactions with CW. Fig. 4 (a) expresses that the characteristic peaks of SEBS located at 2922 cm^{-1}, 2852 cm^{-1}, and 1463 cm^{-1} belong to the vibration of –CH_3, and the peak at 699 cm^{-1} is ascribed to the = CH– bending vibration [43]. OP44E is characterized via absorption peaks of 2953, 2913 and 2847 cm^{-1} that are corresponding to stretching vibration of –CH_3, –CH– and –CH. Absorption peaks at 1470 cm^{-1} and 1369 cm^{-1} refer to bending vibration of –CH_3 and 716 cm^{-1} denotes swinging vibration of –CH_3 [44, 45]. Similar FT-IR spectra of SEBS, OP44E and OP44E/SEBS confirms that SEBS and OP44E are highly compatible in terms of chemical structure. FT-IR spectrum of CW/OP44E/SEBS in Fig. 4 (b) shows that OP44E/SEBS is successfully impregnated in CW confirmed by the characteristic diffraction peaks located at 2953 cm^{-1}, 2916 cm^{-1} and 2849 cm^{-1}. Intensity of these diffraction peaks increases, while intensity of characteristic diffraction peaks located at 1471 cm^{-1} and 717 cm^{-1} decreases, when incorporated to CW/OP44E/SEBS. It can be found that there is no obvious displacement in the characteristic diffraction peaks and no new peaks appear, meaning that no chemical reaction occurs between CW and OP44E/SEBS.

Table 1
Pore parameters of CWs.

Samples	Porosity (%)	Specific surface (m²/g)	Pore volume (mL/g)
CW300	88.6	8.6	9.4
CW500	90.9	9.8	10.9
CW700	90.4	15.8	9.6
CW900	93.5	14.3	15.9

3.2. Thermophysical properties

3.2.1. Phase change temperature and enthalpy of PCMs

The DSC curves of OP44E/SEBS and CW/OP44E/SEBS are shown in Fig. 5. The corresponding melting onset temperature ($T_{o,m}$), latent heat of melting (ΔH_m), solidification onset temperature ($T_{o,c}$) and latent heat of solidification (ΔH_c) are summarized in Table 2. Two characteristic peaks can be detected both in the heating and cooling curves of OP44E/SEBS in Fig. 5 (a)–(b). The lower temperature peak corresponds to the solid-solid phase transition of OP44E, whereas the peak at slightly higher temperature refers to the solid-liquid phase transition [46]. Addition of solid CW has almost no effect on the phase change temperature of composite PCMs. The melting and solidification onset temperatures of composite PCMs are 40.0 and 43.0 °C. The phase change enthalpy is largely dependent on the content of OP44E included in the composite PCMs. It is specific that the enthalpy of composite PCMs is around 200 J/g. The calculated and measured adsorption rates of $\eta_{ads,c}$ and $\eta_{ads,m}$ are determined based on Eqs. (1) and (2) [47,48]. The contents of OP44E/SEBS in composite PCMs are nearly all over 90 %, except the CW900/OP44E/SEBS. This result finely coincides with the pores parameters of CWs listed in Table 1.

$$\eta_{ads,c} = \frac{m_{CW/OP44E/SEBS} - m_{CW}}{m_{CW/OP44E/SEBS}} \tag{1}$$

$$\eta_{ads,m} = \frac{\Delta H_{CW/OP44E/SEBS,m} + \Delta H_{CW/OP44E/SEBS,c}}{\Delta H_{OP44E/SEBS,m} + \Delta H_{OP44E/SEBS,c}} \tag{2}$$

3.2.2. Thermal conductivity of PCMs

The measured values of thermal conductivity of PCMs are shown in Fig. 6. OP44E/SEBS obtains thermal conductivity of 0.34 W/(m·K) which is almost identical to that of OP44E (0.35 W/(m·K)), implying that SEBS hardly affect the thermal conductivity of OP44E and can work as a preferable thickener to improve the leakage of liquid OP44E. When being incorporated into CWs, composite PCMs exhibit diverse thermal conductivities according to the CW prepared at various temperatures. The thermal conductivity of CW300/OP44E/SEBS (0.23 W/(m·K)) is lowest and then increases with the augment of CW carbonation temperature, reaching the maximum of 0.40 W/(m·K) in CW700/OP44E/SEBS. Compared to OP44E/SEBS, the thermal conductivity of CW700/OP44E/SEBS is enhanced by 17.6 %. The PCM impregnated into the pores of CW accumulated more heat than that of air in the pores of CW, and this will result in the prepared composite PCMs having a high thermal conductivity [14].

Two factors affect the thermal conductivity of composite PCMs containing CW carbonated at various temperatures. Fig. 2 shows that the carbon content in CW gradually increases with growth of carbonization temperature. High thermal conductivity carbon improves the thermal conductivity of composite PCMs, which leads to composite PCMs having larger thermal conductivity with CW at higher carbonated temperature. It is noteworthy that the thermal conductivity of composite PCMs decreases when the CW carbonization temperature exceeds 700 °C, dropping to 0.36 W/(m·K) at 900 °C. This is due to reduction in terms of adsorption rate of OP44/SEBS in CW900, resulting in more air filled inside CW900, which hinders the perfection of the heat transfer path and increases the thermal resistance between PCM and CW. It is summarized that enhancing the absorption rate of PCMs in the support skeletons is crucial to improve thermal conductivity of composite PCMs, in addition to upgrade thermal conductivity of the support material.

3.3. Stability

3.3.1. Shape stability of PCMs

Fig. 7 (a) shows that both OP44E and OP44E/SEBS are in solid state at 25 °C. OP44E presents a liquid state and loses shape stability when heated above its melting point. The reversible colloidal mixture formed
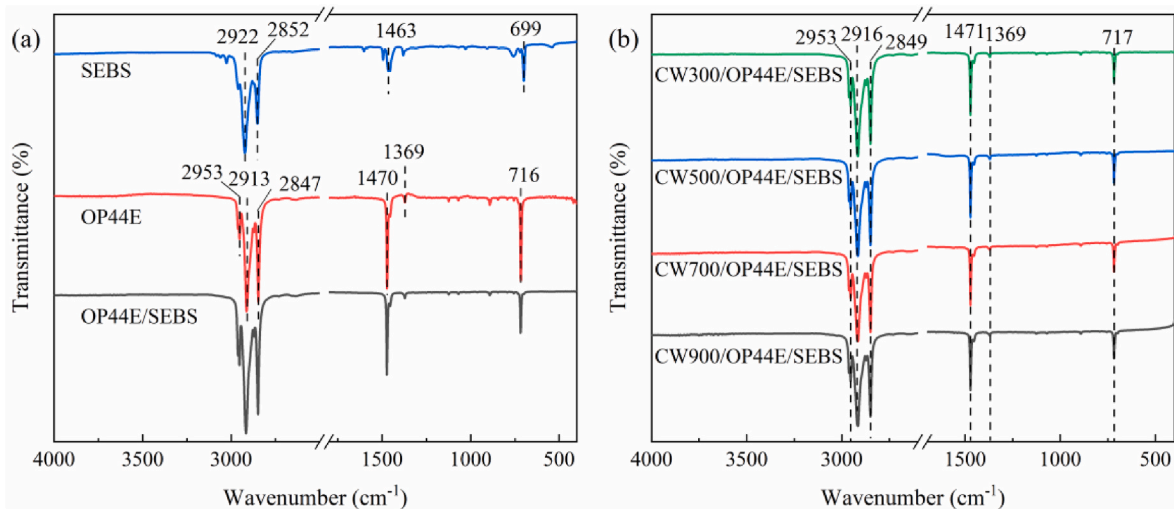
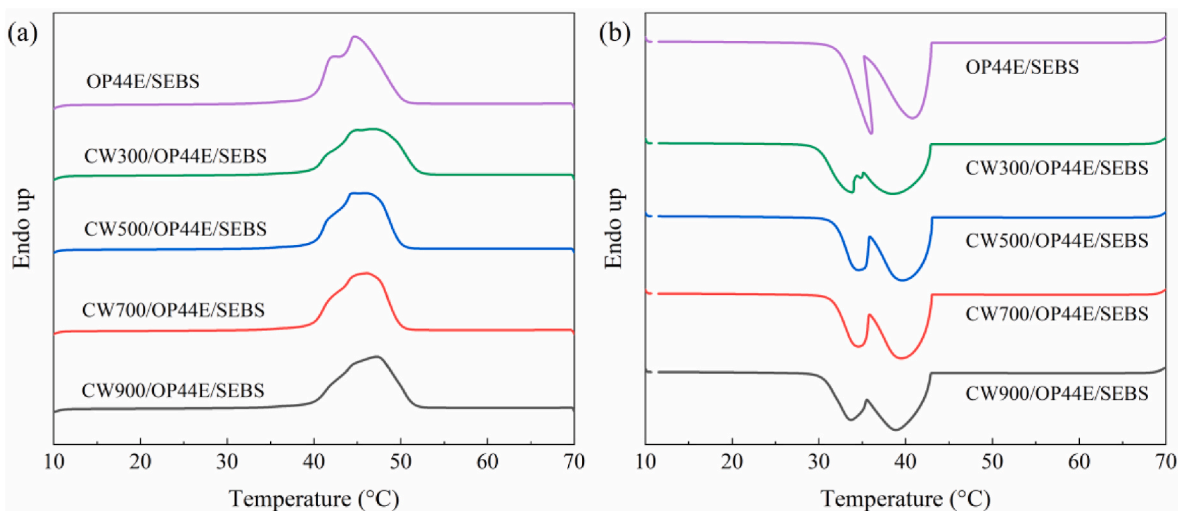**Fig. 4.** FT-IR spectra of PCMs. (a) OP44E/SEBS; (b) CW/OP44E/SEBS.

Fig. 5. DSC curves of PCMs. (a) Melting process; (b) Crystallization process.

Table 2
DSC results of OP44E/SESBS and CW/OP44E/SEBS.

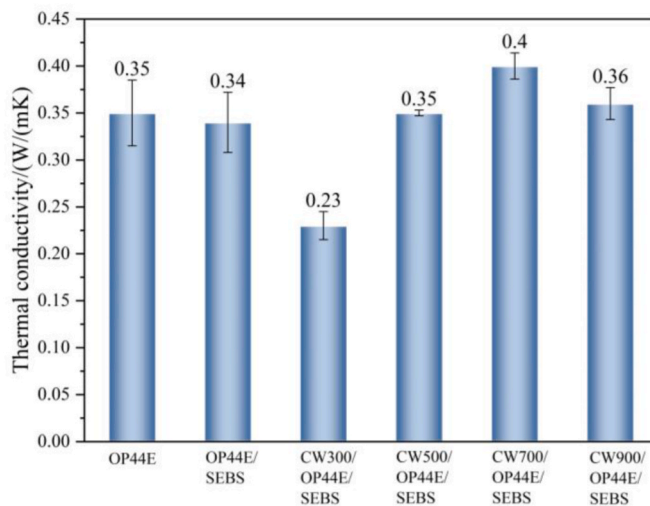| Samples	Melting process		Crystallization process		$\eta_{ads,c}$ (wt.%)	$\eta_{ads,m}$ (wt.%)
	$T_{o,m}$ (°C)	ΔH_m (J/g)	$T_{o,c}$ (°C)	ΔH_c (J/g)		
OP44E	41.5	234.7	43.2	237.3	–	–
OP44E/SEBS	40.1	216.8	42.9	214.0	–	–
CW300/OP44E/SEBS	40.4	195.9	42.9	194.4	93.0	90.6
CW500/OP44E/SEBS	40.3	198.6	43.0	196.6	85.3	91.7
CW700/OP44E/SEBS	40.0	200.6	43.0	199.6	88.6	92.9
CW900/OP44E/SEBS	40.0	191.7	42.9	189.8	91.3	88.6

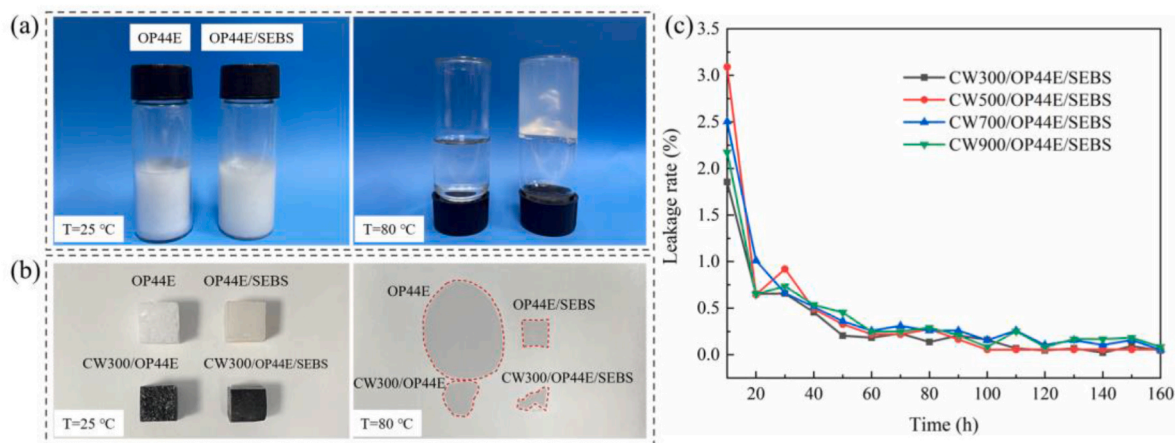**Fig. 6.** Thermal conductivity of PCMs.

Fig. 7. Shape stability of PCMs. (a) Flowability of OP44E and OP44E/SEBS at 25 °C and 80 °C. (b) Leakage of OP44E, OP44E/SEBS, CW300/OP44E and CW300/OP44E/SEBS at 80 °C. (c) Leakage rates of CW/OP44E/SEBSs at 80 °C.

by the compounding of SEBS and OP44E can effectively reduce the flowability of liquid OP44E, which contributes to OP44E/SEBS having a transparent solid gel state without flowing even when it is heated to 80 °C [49]. The OP44E, OP44E/SEBS, and their corresponding composite PCMs adsorbed by CW300 were placed on a paper lay on the 80 °C hot platform and the oil printing areas left on the paper were shown in Fig. 7 (b). It is found that single CW300 hardly prevents the leakage of the liquid OP44E. When coupling with thermoplastic SEBS and being incorporated into hierarchical CW300, OP44E has superior shape stability with a slight leakage observed in surrounding areas. This is caused by a small amount of OP44E/SEBS remained on outside surface. Moreover, Fig. 7 (c) plots the leakage curves of CW/OP44E/SEBS composites at 80 °C within 160 h. Since excess OP44E/SEBS adhered to outside surface of CW, the leakage rates of CW/OP44E/SEBSs are over 2.0 % at the initial stage. With the elapse of time, the leakage rates of composite PCMs then drop sharply. The reduction of leakage rates become mild after heating for 60 h. It is specific that the leakage rates of CW/OP44E/SEBSs are all below 0.2 % at 160 h, implying the admirable shape stability of prepared composite PCMs. The impregnation rates of CW300/OP44E/SEBS, CW500/OP44E/SEBS, CW700/OP44E/SEBS, and CW900/OP44E/SEBS are respectively calculated as high as 93.0 wt %, 85.3 wt%, 88.6 wt% and 91.3 wt% in Table 2, which verifies that CWs can use as supporting and wrapping materials for PCMs.

3.3.2. Cyclic reliability

To investigate the thermally cyclic reliability, composite PCMs were subjected to 200 endothermic/exothermic cycles using a thermostatic metal bath. Only minor leakage is found at the contact surface of the circulation tube that may lead to the reduction of phase change enthalpy. The melting and solidification enthalpies of composite PCMs before and after cycling test are compared in Fig. 8. It is detected that the enthalpies of composite PCMs all decrease obviously with the cyclic time rising from 0 to 100 cycles. Continuing to rise the cyclic time, there merely exists slight decline in enthalpy of composite PCMs. Melting enthalpies of CW300/OP44E/SEBS, CW500/OP44E/SEBS, CW700/OP44E/SEBS and CW900/OP44E/SEBS at 200 cycles are 176.31, 181.74, 180.57 and 178.26 J/g, respectively. Whereas, Fig. 8(b) displays that composite PCMs experiencing 200 cycling tests possess solidification enthalpies of 175.96, 182.05, 181.73 and 183.17 J/g. It is specific that enthalpy of composite PCMs after 200 cycles declines about 10 % in comparison to that without thermal cycling test.

3.3.3. TG analysis

Fig. 9 compares the TG and DTG curves of OP44E/SEBS and CW/OP44E/SEBS composite PCMs. SEBS has higher decomposition temperature than OP44E. Physical mixing of them contributes to the TG curve of OP44E/SEBS having a typical thermal decomposition pattern with two decomposition temperatures. The two decomposition
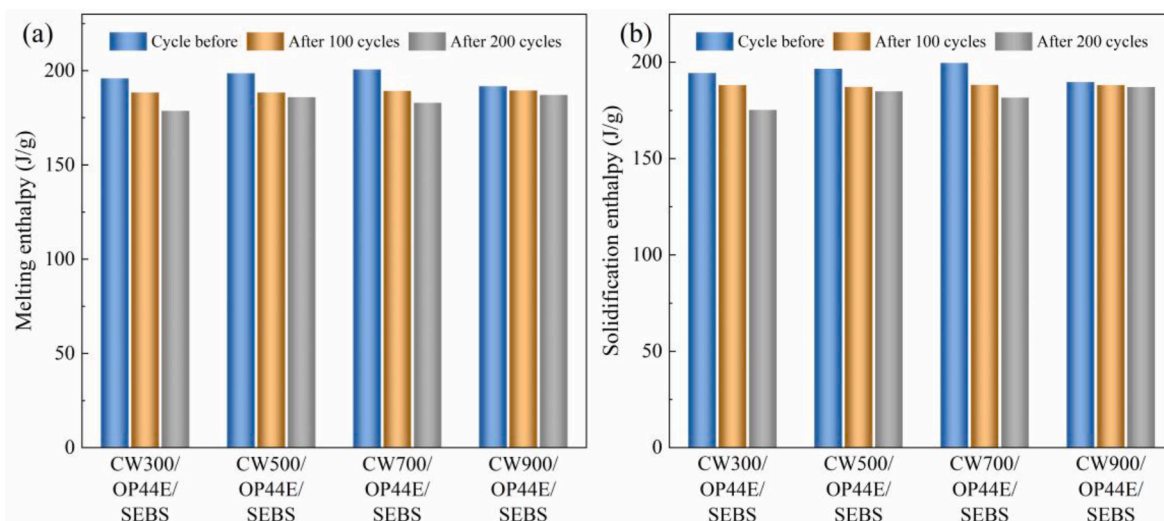

Fig. 8. Enthalpy variation of PCMs in cyclic test. (a) Melting enthalpy and (b) Solidification enthalpy.
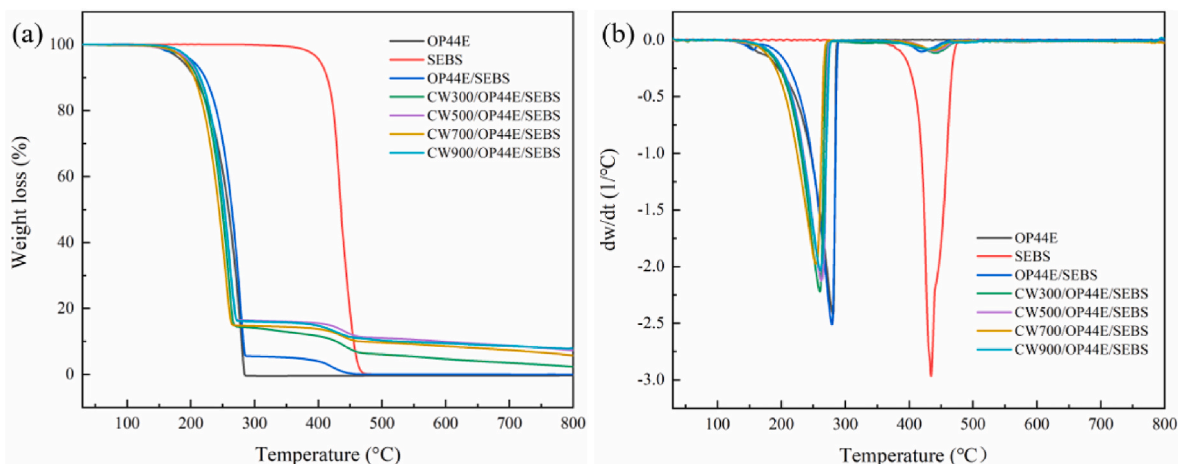
Fig. 9. TG analysis of PCMs. (a) TG curves and (b) DTG curves.

temperatures coincide with the single decomposition steps of OP44E and SEBS, respectively. The first decomposition step at 285 °C is corresponding to the thermal decomposition of OP44E with a residual mass fraction of 5 % at 285 °C, which equals to the mass fraction of SEBS in OP44E/SEBS. The second decomposition step is completed at 467 °C with no residue. Similar to the thermal decomposition pattern of OP44E/SEBS, CW/OP44E/SEBS has two decomposition steps in TG curves. Considering pyrolysis of biomass can be considered as a combination of pyrolysis of three main components: hemicellulose, cellulose, and lignin, the weight loss in the ranges of 220~315 and 315–400 °C is mainly due to the decomposition of hemicellulose and cellulose [50,51]. A residue of about 10 % in composite PCMs at 800 °C is inferred to porous carbon material that has been chemically delignified during the pre-preparation process. TG results testify that the prepared CW/OP44E/SEBS composite PCMs have noticeable thermal stability below 100 °C.

3.4. Photothermal conversion performance

3.4.1. Photothermal conversion efficiency

The photothermal conversion curves of CW/OP44E/SEBS composite PCMs under a xenon lamp radiation are shown in Fig. 10. The temperatures of PCMs rise as the lights turn on and conversely drop as the lights turns off. Fig. 10 displays that the temperature rise curves can be divided into three stages during the light-on period.

(1) The pre-phase change stage. It refers to the time zone before PCMs reach the melting point. Temperatures of PCMs increase significantly with the elapse of time, implying that light radiation can be rapidly converted into thermal energy and stored as sensible heat in PCMs. Higher carbonization temperature of CW produces intense photothermal conversion ability and faster temperature rise rate of PCMs.

(2) The phase change stage. It belongs to the approximate isothermal period that is attributed to the typic phase transition of PCMs. Absorbed thermal energy is stored in the form of latent heat. This stage can store extensive thermal energy within a tiny temperature rise range.

(3) The post-phase change stage. It denotes to the time zone with PCMs temperature larger than their melting points. The temperature of PCMs returns to rise rapidly as the time elapses. CWs convert light radiation into thermal energy that is then stored in PCMs in sensible heat form. Before turning off the xenon lamp, temperatures of CW300/OP44E/SEBS, CW500/OP44E/SEBS, CW700/OP44E/SEBS and CW900/OP44E/SEBS can climb up to 56.8 °C, 60.9 °C, 66.4 °C and 68.2 °C, respectively.

When the xenon lamp turns off, the light-off period can be divided into three stages similar to the light-on period. The PCM temperatures drop sharply with the elapse of time in the pre-phase change stage. PCMs then experience an isothermal phase change stage, followed by a post-phase change stage with temperature dropping rapidly. The photothermal conversion capacity of PCMs can be measured by the photothermal conversion efficiency ($\eta_{P/T}$) which is calculated by Eq. (3).

$$\eta_{P/T} = \frac{m\Delta H_m}{PS(t_t - t_f)} \tag{3}$$

where m is mass of the sample, g; ΔH_m is melting enthalpy of the sample, J/g; P is light radiation intensity of the xenon lamp, W/m^2; S is surface area of the sample subjected to the xenon lamp, m^2; t_t and t_f are the starting and ending time of PCM phase transition, respectively, s.

Based on definition of Eq. (3), Table 3 indicates that the $\eta_{P/T}$ of CW300/OP44E/is calculated as 88.1 %, and increases gradually to 89.5
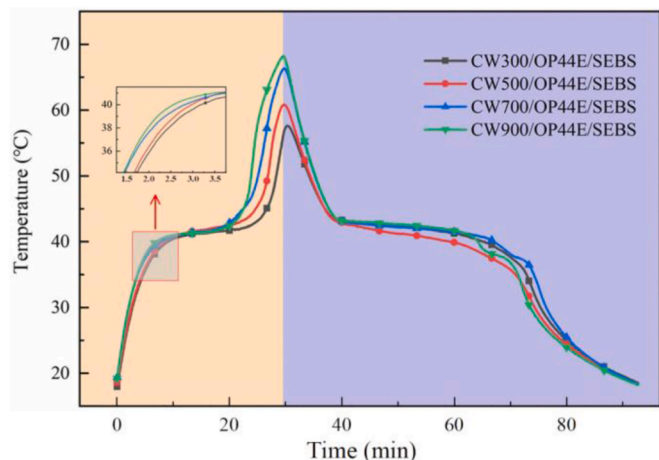

Fig. 10. Transient temperature curves of PCMs.

Table 3
Photothermal conversion efficiency of PCMs.

PCMs	$\eta_{P/T}$ (%)
CW300/OP44E/SEBS	88.1
CW500/OP44E/SEBS	89.5
CW700/OP44E/SEBS	91.0
CW900/OP44E/SEBS	89.4

% and 91.0 % in the CW500/OP44E/SEBS and CW700/OP44E/SEBS, as results of the remarkable photothermal conversion capacity of hierarchical and porous CWs. While, high carbonation temperature damages the CW structure and related photothermal conversion capacity, causing CW900/OP44E/SEBS has $\eta_{P/T}$ of 89.4 % that is lower than those of CW500/OP44E/SEBS and CW700/OP44E/SEBS.

3.4.2. Temperature contour

Considering CW900/OP44E/SEBS has the highest temperature in Fig. 10, this work chooses it as a representative to study the evolution of temperature in the height direction of the composite PCM under the xenon lamp. Fig. 11 (a) describes temperature contour of PCM at various irradiation times under a xenon lamp, gathered by an infrared thermographer. The PCM initial temperature is 22 °C before the xenon lamp turns on. A localized hot zone on the top surface can be observed after 2 min of xenon lamp radiation, which is contributed to the photothermal conversation performance of composite PCM. The hot zone gradually spreads downward through thermal conduction with growth of the irradiation time. The phase transition of PCM occurs accordingly when its temperature is over the melting point. It is discovered that the lowest temperature of the sample is 41.1 °C at 18 min, indicating that the PCM has finished the phase change process.

Fig. 11 (b) shows the axial temperature profiles of PCMs at selected timepoints under xenon lamp radiation. The incident light is reflected several times inside the shallow surface of CW and then is fully absorbed by the porous carbon skeleton. Radiation is quickly transformed into thermal energy, leading to the fact that top surface temperature of PCM is higher than the bulk temperature. The maximal temperatures of PCMs are respectively found as 54.5, 62.0, 70.3, 74.2 and 75.9 °C at 6, 12, 18, 24 and 30 min. As the time elapses, thermal energy accumulated in the shallow layer is transferred downward to the bottom of PCM, by means of thermal conduction. It is obtained in Fig. 6 that CW enables to improve thermal conductivity of PCM, which is conducive to heat conduction. Whereas, thermal conductivity of composite PCM still limits the heat transfer from the top to the bottom. PCM temperature tends to be more uneven with elapse of time. The difference between PCM minimal and maximal temperature is determined as 16.8 °C at 6 min, and then rises to approximately 25.0, 29.2 and 31.6 °C as time elapses to 12, 18 and 24 min. Continuing to extend time induces negative effect to the difference between PCM minimal and maximal temperature (27 °C at 30 min). Fig. 11(b) presents that depths of the hot zones are about 0.323, 0.686, 1.103, 1.716 and 2.000 cm at timepoints of 6~30 min.

3.4.3. Greenhouse experiment

Greenhouse can be termed as a large building with specially designed structure to maximize utilization of solar radiation. The solar radiation passes through the plastic film to heat the indoor air. Considering the low ambient temperature in winter, greenhouse usually suffers from supercooling in winter that is adverse to the plant production. The above investigation indicates that prepared composite PCM has remarkable photothermal conversion and energy storage capacity, which enables to improve the thermal performance of greenhouse theoretically. A small-scale experiment is conducted to analyze effect of photothermal conversion composite PCMs on thermal performance of greenhouse. The xenon lamp (100 mW/cm^2) is employed to simulate solar radiation as shown in Fig. 12 (a). Plants are neglected in the greenhouse in order to simple the experiment. The soil is covered by the plastic film with several K-thermocouples installed inside the greenhouse. Brown wooden board is surrounded outside of the greenhouse set-up to reduce the impact of external light. OP44E/SEBS and CW500/OP44E/SEBS are utilized as PCMs, lay on the soil surface.

Fig. 12 (b) compares the temperature change curves of two PCMs. When the light is on, temperatures of PCMs increase obviously with the elapse of time. The temperature rise rate of CW500/OP44E/SEBS is
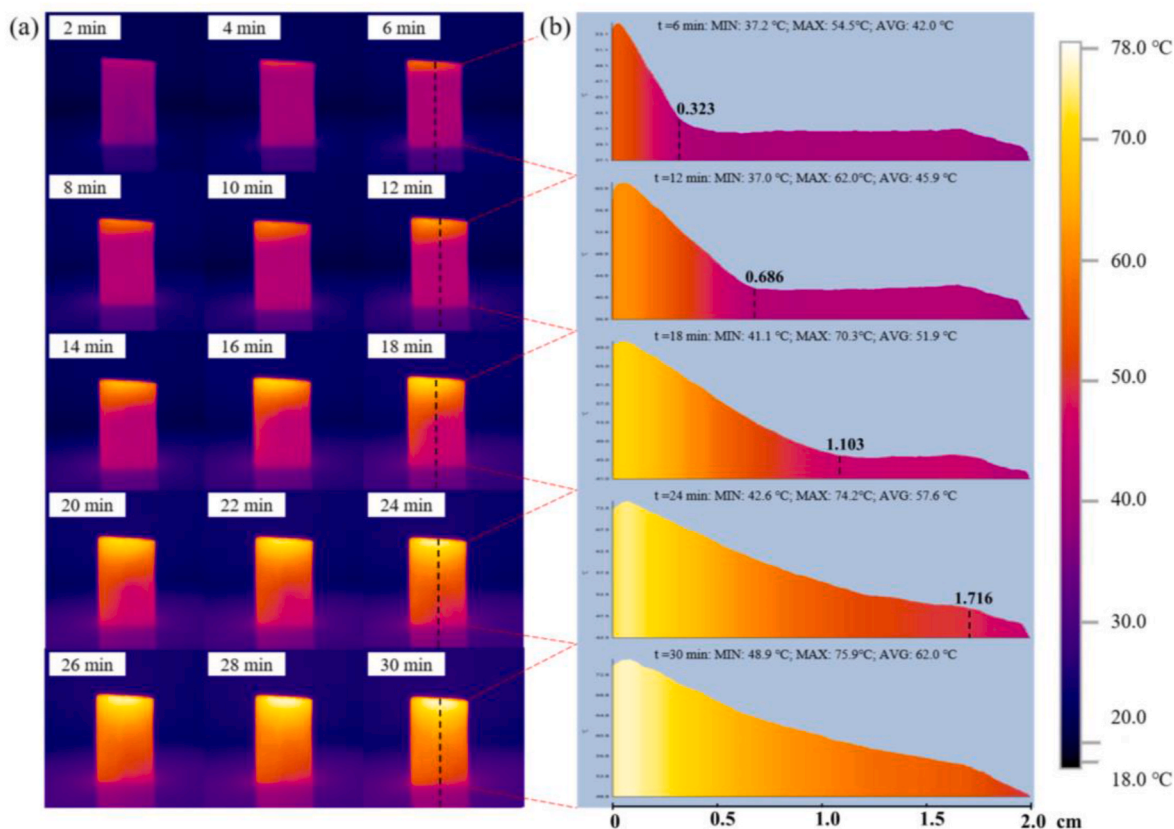

Fig. 11. Temperature variation in the vertical direction of CW900/OP44E/SEBS under xenon lamp. (a) Infrared thermal images at different times (b) Temperature distribution in the height.
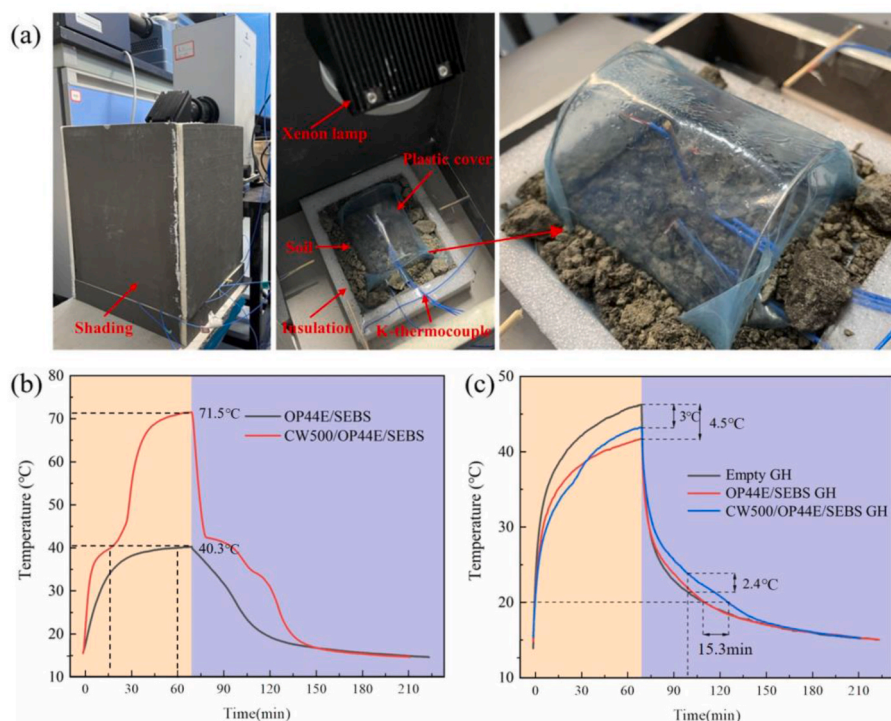
Fig. 12. Greenhouse experiment with PCMs. (a) Experimental set-up; (b) Temperature change curve of PCMs; (c) Temperature change curve of indoor air.

larger than that of OP44E/SEBS, owing to its outstanding photothermal conversion capacity. Light radiation through the plastic film is transformed into thermal energy under the photothermal conversion of CW500/OP44E/SEBS, leading to the rapid temperature increase. Whereas, white surface of OP44E/SEBS has limited absorption and photothermal conversion. OP44E/SEBS mainly relies on the conduction of ambient temperature to gain thermal energy, which results in its low temperature rise. It is specific that temperature of CW500/OP44E/SEBS quickly climbs to its phase change zone, followed by a slow rising stage. After then, its temperature can reach up to 71.5 °C at 70 min. On the contrary, OP44E/SEBS takes longer time to melting and its temperature is merely 40.3 °C at 70 min. When the light is off, temperatures of two PCMs decrease sharply as time elapses. Stored thermal energy is released to warm up the indoor environment of greenhouse. As temperature of CW500/OP44E/SEBS is higher, which producing larger heat transfer temperature difference between PCM and indoor air. Temperature decline rate of CW500/OP44E/SEBS is more obvious than that of OP44E/SEBS. Both temperatures of two PCMs are finally identical to indoor air temperature.

Fig. 12 (c) profiles indoor air temperature change curves of three greenhouses. (empty GH, OP44E/SEBS GH and CW500/OP44E/SEBS GH). It can be seen that the temperatures inside the plastic greenhouses rise substantially with the elapse of time during the light-on period. The empty GH has highest indoor temperature of 46.2 °C after 70 min of the light radiation. The maximal temperatures of CW500/OP44E/SEBS GH and OP44E/SEBS GH are 43.2 and 41.7 °C, which are approximately 3 and 4.5 °C lower in contrast to that of empty GH. The thermal energy storage capacity of PCMs enables to reserve thermal energy transmitted through the greenhouse, producing effective thermal buffering effect. The peak temperature of indoor air is then shaved by the thermal buffering effect. Highlighted photothermal conversion capacity of CW500/OP44E/SEBS rapidly increases its temperature that is significantly higher than the indoor temperature of greenhouse. CW500/OP44E/SEBS starts to heat the air earlier, leading to a higher air temperature inside the greenhouse than the OP44E/SEBS GH. The intersection of indoor temperatures for OP44E/SEBS GH and CW500/

OP44E/SEBS GH appeared at around 33 min implies that CW500/OP44E/SEBS has accomplished the phase transition during the light-on period of 70 min.

The light-off period witnesses indoor temperatures of greenhouses sharply drop with elapse of time, as stored thermal energy is released under indoor temperature below the melting point of PCMs. The empty GH and OP44E/SEBS GH reveal slight inconsistency of indoor temperature curves, meaning that OP44E/SEBS stores limited thermal energy restricted by the poor photothermal conversation capacity. This result well matches with the temperature variation of OP44E/SEBS in Fig. 12 (b). When the light is turned off, indoor temperature of CW500/OP44E/SEBS GH firstly declines to its phase change temperature at the cooling rate identical to those of empty GH and OP44E/SEBS GH. The CW500/OP44E/SEBS then heats the indoor environment through thermal energy released from solidification process, which serves as thermal buffering to slow down the temperature drop of indoor air. The indoor temperature can be shifted via the thermal buffering effect. The duration of maintaining indoor temperature over 20 °C is found to be prolonged by about 15.3 min, in comparison to empty GH and OP44E/SEBS GH cases. This experiment practically confirms the availability of greenhouse temperature controlled by photothermal conversation PCMs, which can provide theoretical support for usage of photothermal conversion PCMs in agriculture.

4. Conclusions

In this work, a series of CWs were prepared by carbonization treatment at different temperatures firstly. And the shape-stable PCMs with photothermal conversion functional were developed by the CWs as supporting material and photothermal conversion media, and OP44E with 5 wt% of SEBS as PCM.

Results indicate that CW has hierarchical and porous structure with the carbon content increasing with augment of carbonization temperature, reaching 94.84 % in terms of CW900. Adsorption of CWs on OP44E/SEBS is over 85 wt% based on vacuum impregnation. Thermal conductivity of composite PCMs can be influenced by CW. Latent heat of

PCMs decreases as the addition of CW that has no phase transition. Composite PCMs have excellent shaping stability and leakage rates of samples are all lower than 0.2 % after 160 h test owing to OP44E/SEBS adhered tightly to the cell wall of CW. Merely 4.6 J/g reduction in enthalpy is observed after 200 endothermic and exothermic cycles. Admirable photothermal conversion of composite PCMs is testified, which is larger than 88 % under a xenon lamp radiation. Temperature contour of composite PCMs indicates that temperature on the shallow layer of PCMs is higher as result of its photothermal conversion capacity. Greenhouse experiment exhibits that CW500/OP44E/SEBS GH gains much higher PCM temperature of 71.5 °C at 70 min, compared to that of 40.3 °C in OP44E/SEBS GH. PCMs enable to exert peak shaving and valley shifting effect on indoor temperature. Maximal indoor temperatures of OP44E/SEBS GH and CW500/OP44E/SEBS GH are reduced by 3 and 4.5 °C compared to the empty GH. Duration of maintaining indoor temperature over 20 °C in CW500/OP44E/SEBS GH is about 15.3 min longer than empty GH and OP44E/SEBS GH cases.

In conclusion, the prepared composite PCMs have improved shaping stability and photothermal conversation capacity, with promising potential to substantial application in the temperature control of agricultural buildings.

CRediT authorship contribution statement

Nan Zhang: Writing – original draft, Methodology, Funding acquisition. **Xiyu Pan:** Writing – original draft, Methodology, Data curation. **Zhaoli Zhang:** Writing – review & editing, Supervision, Conceptualization. **Yanping Yuan:** Writing – review & editing, Supervision, Resources. **Muhammad Sultan:** Writing – review & editing, Supervision, Methodology. **Shady Attia:** Writing – review & editing, Supervision.

Declaration of competing interest

The authors declare that they have no known competing financial interests or personal relationships that could have appeared to influence the work reported in this paper.

Data availability

Data will be made available on request.

Acknowledgments

References

[1] A. Badji, A. Benseddik, H. Bensaha, A. Boukhelifa, I. Hasrane, Design, technology, and management of greenhouse: a review, J. Clean. Prod. 373 (2022) 133753, https://doi.org/10.1016/j.jclepro.2022.133753.

[2] A.M. Pornea, H. Kim, Synthesis of hybrid dual-MOF encapsulated phase-changing material for improved broadband light absorption and photothermal conversion enabling efficient solar energy storage, Sol. Energy Mater. Sol. Cell. 244 (2022) 111817, https://doi.org/10.1016/j.solmat.2022.111817.

[3] W. Sun, X. Wei, B. Zhou, C. Lu, W. Guo, Greenhouse heating by energy transfer between greenhouses: System design and implementation, Appl. Energy 325 (2022) 119815, https://doi.org/10.1016/j.apenergy.2022.119815.

[4] X. Bao, H. Yang, X. Xu, T. Xu, H. Cui, W. Tang, G. Sang, W.H. Fung, Development of a stable inorganic phase change material for thermal energy storage in buildings, Sol. Energy Mater. Sol. Cell. 208 (2020) 110420, https://doi.org/10.1016/j.solmat.2020.110420.

[5] S. Wijesuriya, C. Booten, MarcusV.A. Bianchi, R.A. Kishore, Building energy efficiency and load flexibility optimization using phase change materials under futuristic grid scenario, J. Clean. Prod. 339 (2022) 130561, https://doi.org/10.1016/j.jclepro.2022.130561.

[6] M.M. Ismail, I. Dincer, Y. Bicer, M.Z. Saghir, Effect of using phase change materials on thermal performance of passive solar greenhouses in cold climates, International Journal of Thermofluids 19 (2023) 100380, https://doi.org/10.1016/j.ijft.2023.100380.

[7] J. Zhu, X. Zhang, W. Hua, J. Ji, X. Lv, Current status and development of research on phase change materials in agricultural greenhouses: a review, J. Energy Storage 66 (2023) 107104, https://doi.org/10.1016/J.EST.2023.107104.

[8] I. Sarbu, A. Dorca, Review on heat transfer analysis in thermal energy storage using latent heat storage systems and phase change materials, Int. J. Energy Res. 43 (2019) 29–64, https://doi.org/10.1002/er.4196.

[9] J.M. Mahdi, S. Lohrasbi, E.C. Nsofor, Hybrid heat transfer enhancement for latent-heat thermal energy storage systems: a review, Int. J. Heat Mass Tran. 137 (2019) 630–649.

[10] X. Zhang, Y. Zhang, H. Li, Z. Chen, Enhanced thermal conductivity and photothermal effect of microencapsulated n-octadecane phase change material with calcium carbonate-polydopamine hierarchical shell for solar energy storage, Sol. Energy Mater. Sol. Cell. 256 (2023) 112336, https://doi.org/10.1016/j.solmat.2023.112336.

[11] R. Yang, D. Li, M. Arıcı, B. Wang, Y. Wu, Y. Ma, X. Yang, Photothermal performance of plastic greenhouse embedded with phase change materials in translucent envelopes: a dynamic experimental study, J. Energy Storage 58 (2023) 106375, https://doi.org/10.1016/j.est.2022.106375.

[12] W.T. Le, A. Kankkunen, O.J. Rojas, M.R. Yazdani, Leakage-free porous cellulose-based phase change cryogels for sound and thermal insulation, Sol. Energy Mater. Sol. Cell. 256 (2023) 112337, https://doi.org/10.1016/j.solmat.2023.112337.

[13] P. Singh, R.K. Sharma, M. Khalid, R. Goyal, A. Sarı, V. V Tyagi, Evaluation of carbon based-supporting materials for developing form-stable organic phase change materials for thermal energy storage: a review, Sol. Energy Mater. Sol. Cell. 246 (2022) 111896.

[14] J. Nam, B.Y. Yun, J.Y. Choi, S. Kim, Potential of wood as thermal energy storage materials: different characteristics depending on the hierarchical structure and components, Int. J. Energy Res. 46 (2022) 14926–14945, https://doi.org/10.1002/er.8195.

[15] Y. Sun, N. Zhang, X. Pan, W. Zhong, B. Qiu, Y. Cai, Y. Yuan, Thermal properties of biomass-based form-stable phase change material for latent heat thermal energy storage, Int. J. Energy Res. 45 (2021) 20372–20383, https://doi.org/10.1002/er.7122.

[16] Y. Luo, F. Zhang, C. Li, J. Cai, Biomass-based shape-stable phase change materials supported by garlic peel-derived porous carbon for thermal energy storage, J. Energy Storage 46 (2022) 103929.

[17] Z. Wang, X. Zhang, Y. Xu, G. Chen, F. Lin, H. Ding, Preparation and thermal properties of shape-stabilized composite phase change materials based on paraffin wax and carbon foam, Polymer (Guildf). 237 (2021) 124361.

[18] J. Jacob, A.K. Pandey, N.A. Rahim, J. Selvaraj, J. Paul, M. Samykano, R. Saidur, Quantifying thermophysical properties, characterization, and thermal cycle testing of nano-enhanced organic eutectic phase change materials for thermal energy storage applications, Sol. Energy Mater. Sol. Cell. 248 (2022) 112008, https://doi.org/10.1016/j.solmat.2022.112008.

[19] Z. Yang, Y. Deng, J. Li, Preparation of porous carbonized woods impregnated with lauric acid as shape-stable composite phase change materials, Appl. Therm. Eng. 150 (2019) 967–976.

[20] L. Lv, S. Huang, C. Zhou, W. Ma, Biochar activated by potassium carbonate to load organic phase change material: better performance and environmental friendliness, Ind. Crops Prod. 204 (2023) 117184, https://doi.org/10.1016/j.indcrop.2023.117184.

[21] L. Ma, Q. Wang, L. Li, Delignified wood/capric acid-palmitic acid mixture stable-form phase change material for thermal storage, Sol. Energy Mater. Sol. Cell. 194 (2019) 215–221.

[22] Y. Zhao, B. Sun, P. Du, X. Min, Z. Huang, Y. Liu, X. Wu, M. Fang, Hierarchically channel-guided porous wood-derived shape-stabilized thermal regulated materials with enhanced thermal conductivity for thermal energy storage, Mater. Res. Express 6 (2019) 115515.

[23] W. Chao, H. Yang, G. Cao, X. Sun, X. Wang, C. Wang, Carbonized wood flour matrix with functional phase change material composite for magnetocaloric-assisted photothermal conversion and storage, Energy 202 (2020) 117636.

[24] Y. Li, Y.A. Samad, K. Polychronopoulou, S.M. Alhassan, K. Liao, From biomass to high performance solar–thermal and electric–thermal energy conversion and storage materials, J. Mater. Chem. A Mater. 2 (2014) 7759–7765.

[25] H. Liu, Z. Qian, Q. Wang, D. Wu, X. Wang, Development of renewable biomass-derived carbonaceous aerogel/mannitol phase-change composites for high thermal-energy-release efficiency and shape stabilization, ACS Appl. Energy Mater. 4 (2021) 1714–1730.

[26] M.A. Tony, From biomass residue to solar thermal energy: the potential of bagasse as a heat storage material, EuroMediterr J Environ Integr 5 (2020) 17.

[27] W. Zhang, X. Zhang, Z. Zhang, Z. Yin, Y. Liu, M. Fang, X. Wu, X. Min, Z. Huang, Lauric-stearic acid eutectic mixture/carbonized biomass waste corn cob composite phase change materials: preparation and thermal characterization, Thermochim. Acta 674 (2019) 21–27.

[28] S. Xiao, X. Hu, L. Jiang, Y. Ma, Y. Che, S. Zu, X. Jiang, Nano-Ag modified bio-based loofah foam/polyethylene glycol composite phase change materials with higher photo-thermal conversion efficiency and thermal conductivity, J. Energy Storage 54 (2022) 105238, https://doi.org/10.1016/j.est.2022.105238.

[29] Y. Wei, J. Li, F. Sun, J. Wu, L. Zhao, Leakage-proof phase change composites supported by biomass carbon aerogels from succulents, Green Chem. 20 (2018) 1858–1865.

[30] X. Pan, N. Zhang, Y. Yuan, X. Shao, W. Zhong, L. Yang, Balsa-based porous carbon composite phase change material with photo-thermal conversion performance for thermal energy storage, Sol. Energy 230 (2021) 269–277.

[31] J. Xu, T. Yang, X. Xu, X. Guo, J. Cao, Processing solid wood into a composite phase change material for thermal energy storage by introducing silica-stabilized polyethylene glycol, Compos Part A Appl Sci Manuf 139 (2020) 106098.

[32] Y. Li, X. Li, D. Liu, X. Cheng, X. He, Y. Wu, X. Li, Q. Huang, Fabrication and properties of polyethylene glycol-modified wood composite for energy storage and conversion, Bioresources 11 (2016) 7790–7802.

[33] X. Ye, L. Yang, Z. Tian, P. Zhou, S. Wang, H. Sun, Z. Zhu, J. Li, W. Liang, A. Li, Polypyrrole-coated conjugated microporous polymers/expanded graphene carbon aerogels based phase change materials composites for efficient energy conversion and storage, Sol. Energy Mater. Sol. Cell. 245 (2022) 111873, https://doi.org/10.1016/j.solmat.2022.111873.

[34] B. Chen, M. Han, B. Zhang, G. Ouyang, B. Shafei, X. Wang, S. Hu, Efficient solar-to-thermal energy conversion and storage with high-thermal-conductivity and form-stabilized phase change composite based on wood-derived scaffolds, Energies 12 (2019) 1283.

[35] W. Chen, X. Liang, S. Wang, X. Gao, Z. Zhang, Y. Fang, Macro-encapsulated 3D phase change material: Na2S2O3·5H2O-NaOAc·3H2O/carbonized Melamine sponge composite as core and SiC modified polyurethane thin-layer as shell, Compos. Sci. Technol. 214 (2021) 108981, https://doi.org/10.1016/j.compscitech.2021.108981.

[36] Y. Cai, N. Zhang, X. Cao, Y. Yuan, Z. Zhang, N. Yu, Ultra-light and flexible graphene aerogel-based form-stable phase change materials for energy conversion and energy storage, Sol. Energy Mater. Sol. Cell. 252 (2023) 112176, https://doi.org/10.1016/j.solmat.2022.112176.

[37] Q. Zhang, Y. Zhao, J. Feng, Systematic investigation on shape stability of high-efficiency SEBS/paraffin form-stable phase change materials, Sol. Energy Mater. Sol. Cell. 118 (2013) 54–60, https://doi.org/10.1016/j.solmat.2013.07.035.

[38] T. Wu, Y. Hu, H. Rong, C. Wang, SEBS-based composite phase change material with thermal shape memory for thermal management applications, Energy 221 (2021) 119900, https://doi.org/10.1016/j.energy.2021.119900.

[39] M. Krzesińska, Anisotropy of skeleton structure of highly porous carbonized bamboo and yucca related to the pyrolysis temperature of the precursors, J. Anal. Appl. Pyrolysis 123 (2017) 73–82.

[40] N. Sheng, R. Zhu, K. Dong, T. Nomura, C. Zhu, Y. Aoki, H. Habazaki, T. Akiyama, Vertically aligned carbon fibers as supporting scaffolds for phase change composites with anisotropic thermal conductivity and good shape stability, J. Mater. Chem. A Mater. 7 (2019) 4934–4940.

[41] M. Zhou, J. Wang, Y. Zhao, G. Wang, W. Gu, G. Ji, Hierarchically porous wood-derived carbon scaffold embedded phase change materials for integrated thermal energy management, electromagnetic interference shielding and multifunctional application, Carbon N Y 183 (2021) 515–524.

[42] C. Luo, H. Zhu, W. Luo, F. Shen, X. Fan, J. Dai, Y. Liang, C. Wang, L. Hu, Atomic-layer-deposition functionalized carbonized mesoporous wood fiber for high sulfur loading lithium sulfur batteries, ACS Appl. Mater. Interfaces 9 (2017) 14801–14807.

[43] T. Wu, Y. Hu, H. Rong, C. Wang, SEBS-based composite phase change material with thermal shape memory for thermal management applications, Energy 221 (2021) 119900.

[44] M. Maleki, P.T. Ahmadi, H. Mohammadi, H. Karimian, R. Ahmadi, H.B.M. Emrooz, Photo-thermal conversion structure by infiltration of paraffin in three dimensionally interconnected porous polystyrene-carbon nanotubes (PS-CNT) polyHIPE foam, Sol. Energy Mater. Sol. Cell. 191 (2019) 266–274.

[45] M.M. Umair, Y. Zhang, A. Tehrim, S. Zhang, B. Tang, Form-stable phase-change composites supported by a biomass-derived carbon scaffold with multiple energy conversion abilities, Ind. Eng. Chem. Res. 59 (2020) 1393–1401, https://doi.org/10.1021/acs.iecr.9b06288.

[46] P. Chen, X. Gao, Y. Wang, T. Xu, Y. Fang, Z. Zhang, Metal foam embedded in SEBS/paraffin/HDPE form-stable PCMs for thermal energy storage, Sol. Energy Mater. Sol. Cell. 149 (2016) 60–65, https://doi.org/10.1016/j.solmat.2015.12.041.

[47] G. V Belessiotis, K.G. Papadokostaki, E.P. Favvas, E.K. Efthimiadou, S. Karellas, Preparation and investigation of distinct and shape stable paraffin/SiO2 composite PCM nanospheres, Energy Convers. Manag. 168 (2018) 382–394, https://doi.org/10.1016/j.enconman.2018.04.059.

[48] P.K.S. Rathore, S. kumar Shukla, Improvement in thermal properties of PCM/Expanded vermiculite/expanded graphite shape stabilized composite PCM for building energy applications, Renew. Energy 176 (2021) 295–304, https://doi.org/10.1016/j.renene.2021.05.068.

[49] Q. Zhang, Y. Zhao, J. Feng, Systematic investigation on shape stability of high-efficiency SEBS/paraffin form-stable phase change materials, Sol. Energy Mater. Sol. Cell. 118 (2013) 54–60, https://doi.org/10.1016/j.solmat.2013.07.035.

[50] K. Raveendran, A. Ganesh, K.C. Khilar, Pyrolysis characteristics of biomass and biomass components, Fuel 75 (1996) 987–998, https://doi.org/10.1016/0016-2361(96)00030-0.

[51] T.R. Rao, A. Sharma, Pyrolysis rates of biomass materials, Energy 23 (1998) 973–978, https://doi.org/10.1016/S0360-5442(98)00037-1.